


Lateral Heterostructured Vis-NIR Photodetectors with Multimodal Detection for Rapid and Precise Classification of Glioma

Journal Article

Author(s):

Xie, Hongfei; Pan, Qi; Wu, Dongdong; [Qin, Feifei](#) ; Sun, Wei; Xu, Yang; Chen, Sisi; Wu, Tingqing; Chi, Jimei; Huang, Zengqi; Wang, Huadong; Zhang, Zeying; Chen, Bingda; Carmeliet, Jan; Su, Meng; Song, Yanlin

Publication date:

2022-10-25

Originally published in:

ACS Nano 16(10), <https://doi.org/10.1021/acsnano.2c06004>

Lateral Heterostructured Vis–NIR Photodetectors with Multimodal Detection for Rapid and Precise Classification of Glioma

Hongfei Xie, Qi Pan,* Dongdong Wu, Feifei Qin, Shuoran Chen, Wei Sun, Xu Yang, Sisi Chen, Tingqing Wu, Jimei Chi, Zengqi Huang, Huadong Wang, Zeying Zhang, Bingda Chen, Jan Carmeliet, Meng Su,* and Yanlin Song*



Cite This: *ACS Nano* 2022, 16, 16563–16573



Read Online

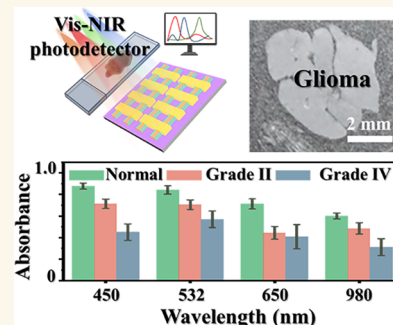
ACCESS |

Metrics & More

Article Recommendations

Supporting Information

ABSTRACT: Precise diagnosis of the boundary and grade of tumors is especially important for surgical dissection. Recently, visible and near-infrared (Vis–NIR) absorption differences of tumors are demonstrated for a precise tumor diagnosis. Here, a template-assisted sequential printing strategy is investigated to construct lateral heterostructured Vis–NIR photodetectors, relying on the up-conversion nanoparticles (UCNPs)/perovskite arrays. Under the sequential printing process, the synergistic effect and co-confinement are demonstrated to induce the UCNPs to cover both sides of the perovskite microwire. The side-wrapped lateral heterogeneous UCNPs/perovskite structure exhibits more satisfactory responsiveness to Vis–NIR light than the common fully wrapped structure, due to sufficient visible-light-harvesting ability. The Vis–NIR photodetectors with R reaching 150 mA W^{-1} at 980 nm and 1084 A W^{-1} at 450 nm are employed for the rapid classification of glioma. The detection accuracy rate of 99.3% is achieved through a multimodal analysis covering the Vis–NIR light, which provides a reliable basis for glioma grade diagnosis. This work provides a concrete example for the application of photodetectors in tumor detection and surgical diagnosis.



KEYWORDS: lateral heterostructure, Vis–NIR photodetectors, multimodal detection, printing, glioma diagnosis

Intelligent photoelectric materials with the advantages of high sensitivity and biocompatibility can be applied to the diagnosis of tumors,^{1,2} such as highly infiltrative and invasive glioma.^{3,4} The high incidence and mortality of glioma require an effective and rapid method for precise diagnosis, especially for its invasive growth and vague boundary in the brain.^{5,6} Currently, the methods for clinical glioma diagnosis are mainly magnetic resonance imaging (MRI) and positron emission tomography (PET).^{7–10} MRI possesses excellent soft-tissue contrast and high spatial resolution but limited sensitivity and accuracy in differentiating glioma grades.^{7,9} Despite the high sensitivity, PET has some disadvantages, such as complex manipulation, poor isotope stability *in vivo*, and limited recognition specificity of the tracer.^{7,10} The emergence of hybrid PET–MRI also brings the disadvantages of operational complexity, high cost, and technical problems.^{7,11,12} Thus, there is an urgent need to develop alternative glioma diagnostic strategies with simple operation, low cost, and high accuracy.

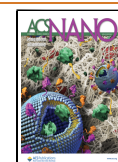
Recently, tissue optical properties vary with the degree of cancer or tissue lesion severity,^{13,14} which have the potential to

aid in the diagnosis of glioma. In most cases, investigations on the tissue optics focus solely on the near-infrared (NIR) region for deep tissue penetration.^{15,16} The differences of morphology and composition in different tissues can also cause the specificity of light absorption in the visible region.^{17–19} It should be noted that the combination of multimodal detection covering the visible and near-infrared light is more suitable for glioma diagnosis, which facilitates guiding the surgery and therapy accurately. Thus, variations in the components of diseased tissues affect the light absorption across the visible and NIR region, which provide a means for characterizing the pathological change, especially for the invasive glioma. There is an urgent need for portable and easy-to-use optoelectronics for

Received: June 18, 2022

Accepted: October 4, 2022

Published: October 6, 2022



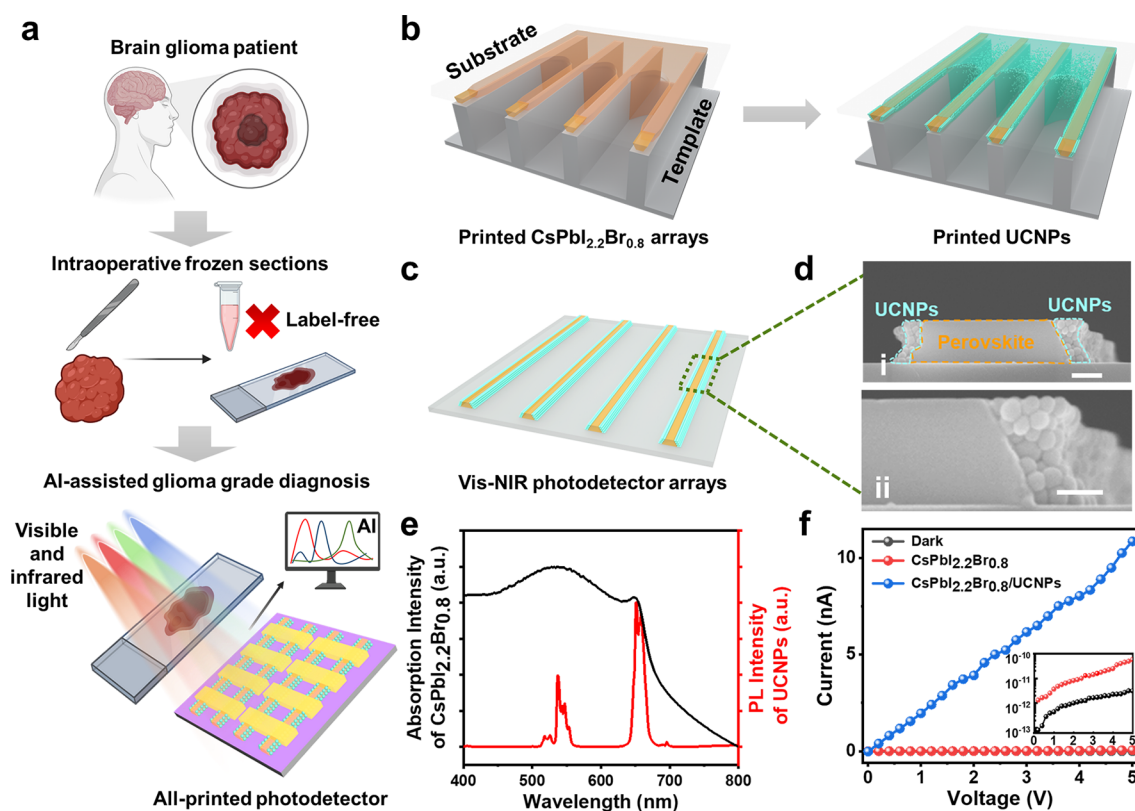


Figure 1. Printed Vis–NIR CsPbI_{2.2}Br_{0.8}/UCNPs photodetector arrays for glioma grade diagnosis. (a) Schematic illustration of the label-free glioma grade diagnosis utilizing printed lateral heterostructured Vis–NIR photodetectors. (b) Schematic process of printing CsPbI_{2.2}Br_{0.8}/UCNPs photodetector arrays. First step: printing CsPbI_{2.2}Br_{0.8} arrays (yellow) by the template-assisted printing strategy; second step: printing UCNPs (green) to form the side-wrapped CsPbI_{2.2}Br_{0.8}/UCNPs 1D structures. (c) Schematic diagram of the Vis–NIR CsPbI_{2.2}Br_{0.8}/UCNPs photodetector arrays. (d) Cross-section scanning electronic microscopy (SEM) images of the 1D side-wrapped CsPbI_{2.2}Br_{0.8}/UCNPs structure. Scale bars, i: 200 nm, ii: 100 nm. (e) Absorption spectra of 1D CsPbI_{2.2}Br_{0.8} arrays and photoluminescence (PL) spectra of UCNPs dispersed in toluene. (f) Dark current and photocurrent of CsPbI_{2.2}Br_{0.8} photodetectors and CsPbI_{2.2}Br_{0.8}/UCNPs photodetectors under the illumination of a 980 nm laser. The inset shows logarithmic *I*–*V* curves of CsPbI_{2.2}Br_{0.8} photodetectors in the dark and under the illumination of a 980 nm laser.

sensing the subtle change of the visible and NIR (Vis–NIR) light to achieve point-of-care diagnostics.

Beyond pristine monolayer and few-layer materials, different species of materials can also be laterally or vertically stacked into heterostructures, which offer a universal route to artificially create hybrid materials to expand the optical sensing capability of photodetectors.^{20–24} Traditional heterostructure construction methods, such as mechanical stripping and stacking, hinder their practical application due to the poor scalability.^{25,26} Thus, solution-processed heterostructures are anticipated as an alternative strategy for scaling applications.^{26,27} Benefiting from the excellent properties of solution processability and high light absorption efficiency, halide perovskites have been widely applied in various photodetectors.^{28–31} Limited by the intrinsic property of the bandgap, the spectral response can only range from 300 to 850 nm.^{32,33} Up-conversion materials are of great significance in biomedical applications due to their intrinsic up-conversion luminescent performance converting two or more low-energy photons to a higher-energy photon.^{34–36} Thus, it is promising to integrate the characteristics of perovskite and up-conversion materials to fabricate heterostructured photodetectors with response to Vis–NIR light. However, uncontrollable morphology and mismatched structures during solution processing often cause performance degradation.^{26,37,38} The loss of photon absorption induced by the structural mismatch

between the perovskite and up-conversion materials further causes the lower responsivity in the visible and NIR region.^{39,40}

The key is the design of optimized stacking configurations that consist of the perovskite and up-conversion materials to exhibit enhanced absorption in the visible to NIR regimes.⁴¹ Until now, there are few reports on the structural optimization and feasible strategy at the micro/nanoscale for heterogeneous up-conversion materials/perovskite-based optoelectronics.

In this work, we present a template-assisted sequential printing strategy to construct 1D side-wrapped lateral heterogeneous photodetectors for achieving a Vis–NIR response, which can be used to differentiate tumor boundaries and glioma grade diagnosis. The side-wrapped NaYF₄@Yb, Er nanoparticles/CsPbI_{2.2}Br_{0.8} perovskite-based heterogeneous structure can be constructed by utilizing the synergistic effect and space confinement of the micropillar template and the barrier of the preprinted 1D perovskite arrays. Owing to the excellent light-harvesting ability of Vis–NIR light, the side-wrapped lateral heterogeneous structure exhibits much more excellent responsiveness to Vis–NIR light than the common fully wrapped heterogeneous structure. The side-wrapped lateral heterogeneous photodetectors with *R* reaching 150 mA W^{−1} at 980 nm and 1084 A W^{−1} at 450 nm are achieved. The accuracy of glioma grade diagnosis reaches 99.3% through multimodal detection, demonstrating the ability of glioma grade diagnosis. This work provides an efficient approach for

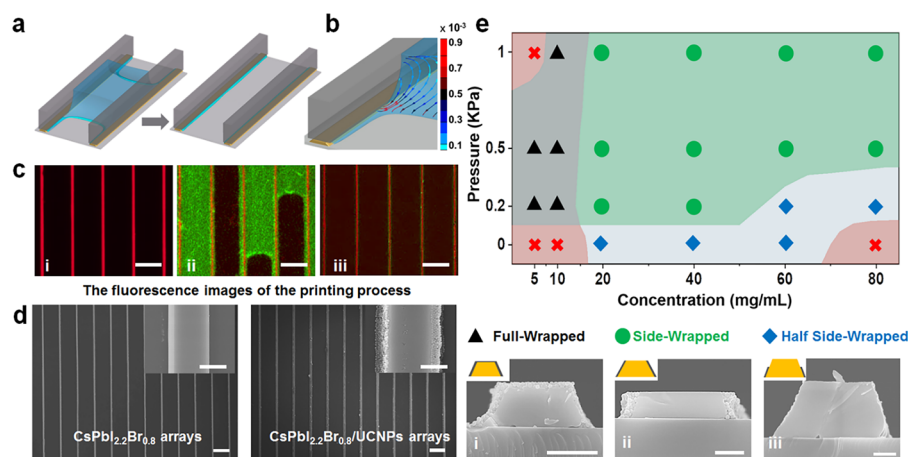


Figure 2. The preparation process and morphology control of the CsPbI_{2.2}Br_{0.8}/UCNPs 1D arrays. (a) Numerical simulation of the flow behavior of UCNP ink confined between the micropillar-structured template and the substrate. The secondary printed UCNPs (blue) are densely distributed on both sides of the first printed trapezoid-structured perovskite microwire (yellow). (b) The flow behavior in the forepart of the liquid bridge during the secondary printing process. (c) *In situ* fluorescent microscopy observation of flow behavior of the UCNP ink. As the solvent is evaporated, the three-phase contact line is receding and the UCNPs are confined to both sides of the perovskite arrays with capillary trailing. Scale bars, 20 μ m. (d) SEM images of the 1D CsPbI_{2.2}Br_{0.8} arrays and 1D of CsPbI_{2.2}Br_{0.8}/UCNPs arrays. Insets of (d) are magnified SEM images, respectively. Scale bars, 20 μ m. Inset of (d), 1 μ m. (e) Phase diagram of different CsPbI_{2.2}Br_{0.8}/UCNPs heterostructures versus the concentration of the CsPbI_{2.2}Br_{0.8} precursor solution and the pressure applied to the printing system. Cross-section SEM images of the fully wrapped structure (i), the side-wrapped structure (ii), and half side-wrapped structure (iii). Scale bars, 500 nm.

the fabrication of a portable photoelectronic device and the application of surgical diagnosis.

RESULTS AND DISCUSSION

Design of UCNPs/Perovskite Vis–NIR Photodetectors for Glioma Diagnosis. Figure 1a demonstrates the schematic illustration of the glioma diagnosis utilizing the Vis–NIR photodetectors. Owing to the difference in the absorbance of different grades of glioma, the response of the transmitted light from the histopathologic section at different wavelengths can be employed to distinguish the grade of glioma. The machine learning algorithm-assisted analysis will further improve the accuracy of glioma grade diagnosis. The Vis–NIR photodetectors, obtained via a template-assisted sequential printing strategy, consist of perovskite arrays and UCNPs wrapped on both sides of the perovskite arrays. The perovskite arrays are fabricated by constructing a sandwich printing system of the substrate, ink, and template.⁴² Due to the hydrophilic state of the substrate and the capillary force, the precursor solution is easily filled and confined between the tops of the template and the target substrate. The template is modified with hydrophobic 1*H*,1*H*,2*H*,2*H*-perfluorodecyltrimethoxysilane to guarantee the shrinkage and segmentation of the liquid film and the construction of the trapezoidal structure. Driven by the Laplace pressure difference, the three-phase contact line shrinks.⁴³ The liquid film is divided into the individual liquid column with uniform size and regular orientation under the guidance of the micropillars. With the further evaporation of the solvent, the perovskite precursor solution in the liquid column tends to be supersaturated. Consequently, the perovskite nucleates, crystallizes, and grows along the micropillar of the template (Figure 1b). 1D perovskite arrays with consistent size and strict alignment are obtained after total evaporation of the solvent. Subsequently, the UCNP ink, prepared from the antisolvent of the printed perovskite arrays, is continuously injected along the orientation of the micro-

pillars. Similarly, due to the evaporation of the solvent and the shrinkage of the three-phase contact line, the UCNPs accompanied by capillary trailing are deposited on both sides of the perovskite arrays (Figure 1b). Finally, the 1D UCNPs/perovskite side-wrapped lateral heterogeneous photodetector arrays are fabricated on the substrate as the solvent evaporates completely (Figure 1c). Figure 1d shows the scanning electron microscopy (SEM) images of the cross-section of the UCNPs/perovskite lateral heterogeneous structure. The UCNPs (Figure S1) are only densely distributed on both sides of the trapezoid-structured perovskite microwire due to the co-confinement of templates and the first printed perovskite array.

Lanthanide (Ln)-doped rare-earth NaYF₄@Yb, Er nanoparticles are employed to convert NIR light to visible light from the rich energy-level structure of trivalent lanthanide ions.³⁴ CsPbI_{2.2}Br_{0.8} is employed after the bandgap engineering to match the absorption band with the up-conversion luminescent (UCL) band of the UCNPs (Figure S2).^{44,45} Figure 1e shows the photoluminescent (PL) spectrum of UCNPs dispersed in toluene excited at 980 nm and the absorption spectrum of CsPbI_{2.2}Br_{0.8} arrays. The UCNPs show UCL peaks at 520, 540, and 654 nm, which can be assigned to ⁴H_{11/2} → ⁴I_{15/2}, ⁴S_{3/2} → ⁴I_{15/2}, and ⁴F_{9/2} → ⁴I_{15/2} transitions of erbium, respectively (Figure S3).³⁴ The infrared response of UCNPs/CsPbI_{2.2}Br_{0.8} heterogeneous photodetectors relies on the introduction of UCNPs. The CsPbI_{2.2}Br_{0.8} microwires do not show any emission peak under the excitation at 980 nm, while the UCNPs/CsPbI_{2.2}Br_{0.8} microwires show distinct peaks whose positions are the same as that of the UCNPs (Figure S4). The UCL of 520, 540, and 654 nm can be effectively absorbed by the CsPbI_{2.2}Br_{0.8} microwire for the narrower bandgap (1.86 eV).⁴⁶ Thus, attributed to the overlap between the UCL spectrum of UCNPs and the absorption spectrum of the CsPbI_{2.2}Br_{0.8} arrays, the 1D CsPbI_{2.2}Br_{0.8}/UCNPs heterogeneous structure can respond to both visible and NIR light. The infrared response of pristine CsPbI_{2.2}Br_{0.8} perovskite

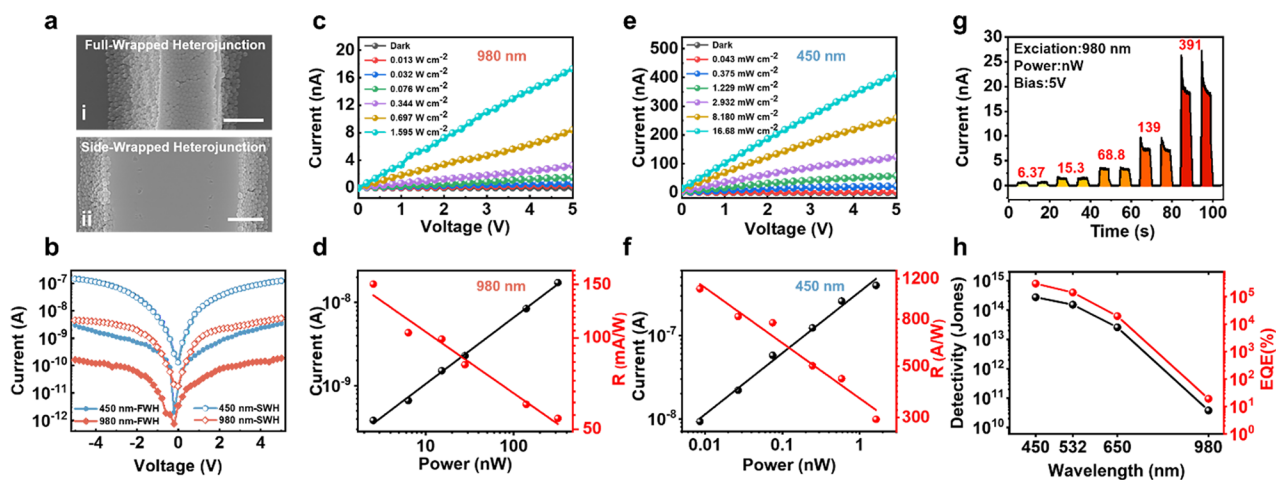


Figure 3. Vis–NIR photoresponse performance of CsPbI_{2.2}Br_{0.8}/UCNPs heterogeneous photodetectors. (a) SEM images of fully wrapped CsPbI_{2.2}Br_{0.8}/UCNPs 1D heterojunction (i) and side-wrapped CsPbI_{2.2}Br_{0.8}/UCNPs 1D heterojunction (ii). Scale bars, 500 nm. (b) Logarithmic *I*–*V* curves of fully wrapped heterojunction (FWH) and side-wrapped heterojunction (SWH) under the illumination of 450 and 980 nm. (c) *I*–*V* curves of the side-wrapped heterogeneous photodetectors in the dark condition and under different illumination powers of a 980 nm laser. (d) Photocurrent and responsivity of the side-wrapped heterogeneous photodetectors under different incident power of 980 nm laser. (e) *I*–*V* curves of the side-wrapped heterogeneous photodetectors in the dark and under different illumination powers of a 450 nm laser. (f) Photocurrent and responsivity of the side-wrapped heterogeneous photodetectors under different incident powers of a 450 nm laser. (g) *I*–*t* response of the side-wrapped heterogeneous photodetectors under different illumination powers of a 980 nm laser. (h) The highest detectivity and external quantum efficiency of the side-wrapped heterogeneous photodetectors under the illumination of different wavelengths (450, 532, 650, and 980 nm).

arrays and CsPbI_{2.2}Br_{0.8}/UCNPs arrays at an illumination power density of 0.85 W cm^{−2} is shown in Figure 1f. The pristine CsPbI_{2.2}Br_{0.8} arrays exhibit very low photocurrent (5.74×10^{-11} A) under 980 nm light illumination. The CsPbI_{2.2}Br_{0.8}/UCNPs arrays show significantly enhanced photocurrent (1.08×10^{-8} A), which is 188 times higher than that of the pristine perovskite with the same illumination power at a drain voltage of 5 V. It is worth mentioning that the wrapped UCNPs will not significantly affect the response of the perovskite to visible light because of the side-wrapped structure. There is little difference between the photocurrent of the CsPbI_{2.2}Br_{0.8}/UCNPs microwire (496 nA) and CsPbI_{2.2}Br_{0.8} microwire (522 nA) under the illumination power (18.20 mW cm^{−2}) of a 450 nm laser (Figure S5). The lateral heterostructured CsPbI_{2.2}Br_{0.8}/UCNPs can broaden the response band to the infrared band without affecting the intrinsic visible-band response of the perovskite.

Preparation of 1D UCNPs/Perovskite Arrays. To demonstrate the fluid flow behavior of UCNP ink during the secondary printing process, a pseudopotential two-phase lattice Boltzmann model combined with a nanoparticle transport model is applied to simulate the hydrodynamic behavior of UCNP ink.^{47,48} The evaporation occurring at the two open ends of the channel is induced by a pressure difference between the saturated vapor pressure at the liquid–gas interface and the open ends. Owing to the difference in the wettability between the substrate and the template (Figure S6), the liquid bridge in contact with the substrate shrinks more slowly. The UCNPs are aggregated at the front end of the meniscus in contact with the substrate. The liquid film remains due to the capillary flow from the bulk, which can be termed as capillary trailing.⁴⁹ Due to the co-confinement of the first printed perovskite arrays and the template, capillary trailing only remains on both sides of perovskite microwires during the meniscus shrinking. As a result, the UCNPs are distributed on both sides of the perovskite microwire as the solvent

evaporates completely (Figure 2a and Figure S7 and Movie S1). The flow lines of the capillary trailing are shown in Figure 2b, where the arrows illustrate the direction of the fluid flow. The UCNP ink flows to the capillary trailing in contact with the substrate and the perovskite arrays, confirming that UCNPs will be deposited on both sides of the perovskite structure. *In situ* fluorescent microscopy observation is also performed to visualize the printing process of the CsPbI_{2.2}Br_{0.8}/UCNPs arrays. Figure 2c–i–iii show the fluorescence images of the perovskite arrays, the shrinkage of the UCNPs liquid, and the CsPbI_{2.2}Br_{0.8}/UCNPs arrays, respectively. The detail of the sequential printing process is recorded in Figure S8. Figure 2d–i and Figure S9 show the SEM and fluorescence microscope images of the CsPbI_{2.2}Br_{0.8} perovskite arrays with strict alignment and a smooth surface. The representative image of the CsPbI_{2.2}Br_{0.8}/UCNPs microwire shows that the UCNPs are only densely distributed on both sides of the perovskite (inset of Figure 2d–ii). The energy-dispersive X-ray spectrometry (EDS) mapping images confirm that the Na, F, and Y elements are only distributed on both sides of the CsPbI_{2.2}Br_{0.8} microwire (Cs, Pb, I, and Br elements), suggesting the successful fabrication of the 1D CsPbI_{2.2}Br_{0.8}/UCNPs side-wrapped lateral heterogeneous structure (Figure S10).

Morphology Control of UCNPs/Perovskite Heterostructures. The morphology of the CsPbI_{2.2}Br_{0.8}/UCNPs heterogeneous structure is controlled by the liquid flow behavior of UCNP inks during the sequential printing process, which is affected by the concentration of the perovskite precursor solution and the pressure applied to the printing system. It is noted that successful printing can be achieved easily when a certain pressure is applied to the printing system. Printed 1D perovskite arrays can only be obtained on the substrate with appropriate contact angles at fixed temperatures and without extra applied pressure (Figure S11). However, the perovskite arrays can be obtained easily when the printing

system is applied with proper pressure (>0.5 KPa). The gap between the template and the substrate can stay uniform during the liquid shrinkage process under pressure, which is beneficial to the stable shrinkage of the liquid bridge. Figure S12 shows the uniform height of the perovskite microwires under pressure, which is the prerequisite for printing uniform CsPbI_{2.2}Br_{0.8}/UCNPs arrays. Figure 2e shows the phase diagram of different heterostructures versus the concentration of the CsPbI_{2.2}Br_{0.8} precursor solution and the pressure applied to the printing system. All the points in the diagram are obtained at the same ambient temperature and the same contact angle of the substrate and the template. To obtain the side-wrapped lateral heterogeneous structure, the width and the height of the perovskite arrays should be regulated appropriately to ensure the UCNPs are wrapped on the sides of the perovskite arrays. The width of the perovskite microwire can be controlled by changing the concentration of the perovskite precursor solution. The width (*W*) increased from 755 nm to 2.51 μm with the concentration changing from 5 mg mL⁻¹ to 80 mg mL⁻¹ (Figure S13). When the width of the perovskite microwire is large (*W* > 1.0 μm), the UCNP ink cannot cross over the microwire, forming the side-wrapped lateral heterogeneous structure. However, the perovskite microwire with a small width (*W* < 1.0 μm) cannot prevent the UCNP ink from covering both sides and the top of the perovskite microwire during the sequential printing process. Thus, the top and both sides of the perovskite arrays will be covered by UCNPs (Figure 2e-i). The height of the perovskite arrays can be tuned by changing the pressure applied to the printing system. When the applied extra pressure changes from 0 KPa to 1 KPa, the height (*H*) of perovskite arrays decreases from 1.41 μm to 245 nm (Figure S13). When the height of the perovskite microwire obtained by the first assembly process is lower (*H* < 1.2 μm), the UCNPs can cover the sidewall of the perovskite microwire totally (Figure 2e-ii). When the height is relatively higher (*H* > 1.2 μm), UCNPs cannot completely occupy the sidewall of the perovskite microwire (Figure 2e-iii).

Characterization of Optoelectronic Performances.

The Vis–NIR photodetectors are fabricated by depositing a 100 nm Au layer on 1D CsPbI_{2.2}Br_{0.8}/UCNPs arrays using thermal evaporation through a mask.³⁰ The photoresponse difference of a side-wrapped CsPbI_{2.2}Br_{0.8}/UCNPs heterojunction (SWH) and a fully wrapped CsPbI_{2.2}Br_{0.8}/UCNPs heterojunction (FWH) to visible light and infrared light (980 nm) is investigated. The photocurrents of the side-wrapped CsPbI_{2.2}Br_{0.8}/UCNPs heterojunction at 450 and 980 nm are 1.25 × 10⁻⁷ A and 5.40 × 10⁻⁹ A, respectively, which is 36 times (fully wrapped heterojunction, 3.43 × 10⁻⁹ A@455 nm) and 29 times (fully wrapped heterojunction, 1.86 × 10⁻¹⁰ A@980 nm) those of the fully wrapped CsPbI_{2.2}Br_{0.8}/UCNPs heterojunction under the same illumination power (Figure 3a,b). The wrapped UCNPs weaken the absorption of visible light. On the other hand, the blocking of UCNPs in the fully wrapped CsPbI_{2.2}Br_{0.8}/UCNPs structure causes poor ohmic contact between electrodes and the perovskite microwires. Therefore, the side-wrapped CsPbI_{2.2}Br_{0.8}/UCNPs structure satisfies the light absorption efficiency in both the visible and infrared regions.

Besides, the wrapped width of UCNPs is investigated to achieve the optimal performance for the light detection. As shown in Figure S14, the side-wrapped heterostructure with different wrapped width from about 50 to 400 nm can be obtained by adjusting the concentration of the secondary

printed UCNP ink. The infrared response performance benefits from the luminescence intensity of the wrapped UCNPs. Compared with the wrapped width of 50 nm, the heterostructure with a wrapped width of 200 nm possesses more UCNPs for sufficient luminescence, resulting in a stronger infrared response. However, when the wrapped width is too large (400 nm), the infrared and visible response performance deteriorated due to the poor contact between electrodes and the perovskite wires (Figure S14). Therefore, the UCNPs/perovskite photodetectors with the wrapped width of about 200 nm achieve the optimal performance.

For the side-wrapped CsPbI_{2.2}Br_{0.8}/UCNPs photodetectors with optimal wrapped width, the photoresponse performance for the Vis–NIR light is investigated. Figure 3c shows the current–voltage (*I*–*V*) curves under dark and 980 nm light illumination with different incident powers from 0.013 W cm⁻² to 1.595 W cm⁻². The photocurrent is significantly increased under the increasing illumination intensity. The low dark current (9.90 × 10⁻¹² A) observed at the voltage of 5 V indicates a low intrinsic carrier concentration of perovskite. The responsivity (*R*) is calculated by $R = I_{\text{ph}}/P$, where *I*_{ph} is the photocurrent and *P* is the incident light intensity, respectively.⁵¹ Light current and responsivity curves that depend on the incident light power are presented (Figure 3c). Figure 3d shows the relationship among the light power density, photocurrent, and *R*. With the incident 980 nm light power density increasing from 0.013 W cm⁻² to 1.595 W cm⁻², the photocurrent increases significantly from 3.83 × 10⁻¹⁰ A to 1.73 × 10⁻⁸ A. The *R* can reach 150.5 A mW⁻¹ under a light power density of 0.013 W cm⁻². As the incident power increases, the responsivity gradually decreases, which can be ascribed to enhanced exciton recombination at high carrier concentration.⁴⁹ The photoresponse characteristics of the side-wrapped lateral heterogeneous photodetectors are further investigated over typical visible illumination wavelengths (450, 532, and 650 nm) to confirm the excellent visible light response performance of the structure (Figure 3e and Figure S15). The maximum *R* response under excitation at 450, 532, and 650 nm is 1084 A W⁻¹, 604 A W⁻¹, and 102 A W⁻¹, respectively (Figure 3f and Figure S15). The high responsibility and detectivity can be ascribed to both the strict alignment and high crystallinity of the perovskite microwire and the side-wrapped CsPbI_{2.2}Br_{0.8}/UCNPs structure. The *I*–*t* temporal response of the side-wrapped heterogeneous photodetectors is evaluated by two light pulses with gradually increasing laser power and a time interval of 10 s, as shown in Figure 3g and Figure S16. Under the excitation of various wavelengths of light, the photocurrent increases with the increase of the incident power. The printed photodetectors exhibit excellent sensitivity and stability of response to the dynamic change of the illumination.

The detectivity (*D*^{*}) and external quantum efficiency (EQE) of PDs are an important figure-of-merit of photodetectors. The detectivity (*D*^{*}) is obtained by $D^* = \frac{R\sqrt{S}}{\sqrt{2eI_{\text{dark}}}}$, where *S* is the effective area of the device and *I*_{dark} is the dark current of the PDs.⁵¹ The external quantum efficiency (EQE) is calculated according to the following equation: $\text{EQE} = \left(R \frac{hc}{\lambda e} \times 100\right)\%$, where *h* is Planck's constant, *c* is the velocity of light, *λ* is the wavelength of the incident light, and *e* is the elementary charge.⁵¹ Maximum *D*^{*} and EQE at different

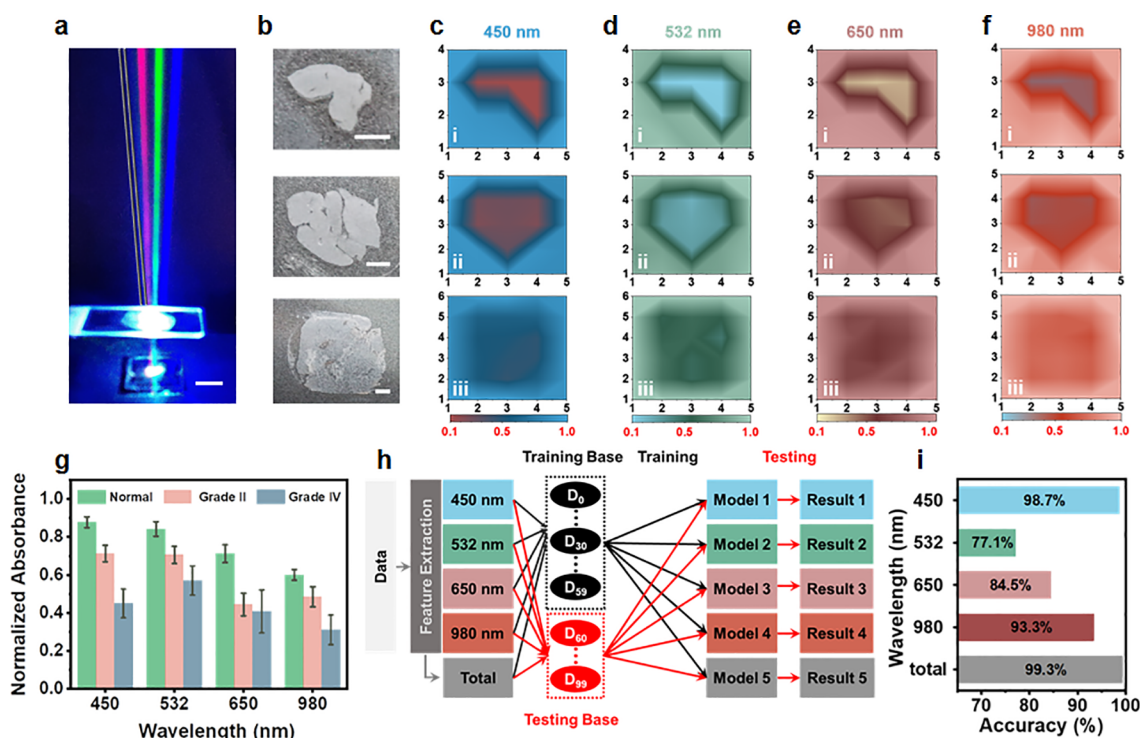


Figure 4. Glioma grade diagnosis ability based on the photoelectric response of the side-wrapped lateral heterogeneous photodetectors. (a) Optical image of the testing system. Lasers of typical wavelengths (450, 532, 650, and 980 nm) were irradiated on the Vis–NIR photodetectors after transmitting through different regions of the tissue sections. Scale bars, 1 cm. (b) Optical images of the normal tissue, grade II glioma tissue, and grade IV glioma tissue. Scale bars, 1 mm. (c–f) Reconstructed imaging of three different tissues by the photoelectric conversion of the side-wrapped heterogeneous photodetectors. The data are normalized by the maximum photocurrent extracted under the illumination of different wavelengths of 450, 532, 650, and 980 nm, respectively. (g) The normalized absorbance histogram of normal tissue, grade II glioma tissue, and grade IV glioma tissue at different wavelengths. (h) The principle of the detection accuracy based on the SVM algorithm. (i) The detection accuracy of glioma diagnosis. Based on the multimodal detection covering the Vis–NIR light, the detection accuracy is improved to 99.3%.

wavelengths are summarized in Figure 3h. The D^* values of the CsPbI_{2.2}Br_{0.8}/UCNPs arrays under excitation at 450, 532, 650, and 980 nm are 2.72×10^{14} , 1.51×10^{14} , 2.58×10^{13} , and 3.78×10^{10} Jones, respectively. The EQE of the CsPbI_{2.2}Br_{0.8}/UCNPs arrays under excitation at 450, 532, 650, and 980 nm are 299.414%, 141.095%, 19.586%, and 19.1%, respectively. The large EQE is attributed to the excellent photoresponsivity of the Vis–NIR photodetectors. The response time is obtained with the current increasing from 10% to 90% for rising and decreasing from 90% to 10% for decay.⁵¹ As shown in Figure S17, the response time of the side-wrapped heterogeneous photodetectors is 6.31 ms for the rise and 6.39 ms for the decay. The satisfactory optoelectronic properties of visible light and NIR light are mainly attributed to the side-wrapped structure. Thus, the light response of the side-wrapped lateral heterogeneous structure is much better than the fully wrapped structure.

Glioma Grade Diagnosis. The accurate judgment for the boundary and invasive growth of glioma in the brain is the premise of precise diagnosis and treatment. The cell morphology and component of the normal brain tissues and different grades of glioma are inconsistent and dynamically changing, which leads to differences in their absorption of light at different wavelengths.^{14,17} Based on the sensitive photoelectric response in the wide band, our Vis–NIR photodetectors can be employed to distinguish normal tissues from glioma, as well as glioma grades.

The glioma information can be converted into electrical signals collected by Vis–NIR photodetectors, which is beneficial for the rapid and precise diagnosis of glioma. A simple microscopic test system can be built to perform the grading diagnosis of glioma (Figure 4a). Typical wavelengths of laser lights (450, 532, 650, and 980 nm) are irradiated on the Vis–NIR photodetectors after transmitting through different regions of the tissue sections. Figure 4b shows the optical photos of normal tissue, grade II glioma tissue, and grade IV glioma tissue, respectively. Normal tissue, grade II glioma tissue, and grade IV glioma tissue are isometrically divided into matrix regions. Every region is illuminated by laser lights with different wavelengths. The contour images of different tissue sections are obtained by normalizing the photocurrents of typical regions at 450, 532, 650, and 980 nm, respectively (Figure 4c–f). The number of pixels of the contour images can reach $400 \text{ pixels cm}^{-2}$. Based on the high performance of the photoelectric response, the reconstructed contour maps are nearly identical to the physical maps of different tissues, indicating the potential for tissue boundary identification. Under the irradiation of four typical wavelengths, the photocurrents of normal tissue are significantly weaker than that of grade II and grade IV glioma. This distinction suggests that the device can differentiate between normal and glioma tissue. As the incident light changes from the visible region to the NIR region, the photocurrents of different tissues increase gradually, which also confirms the penetrating capability of NIR light. Figure 4g shows the

normalized absorbance statistics histogram of normal tissue, grade II glioma, and grade IV glioma at different wavelengths. Obvious differences in the absorption of different light by different tissues are observed from Figure 4g, which can be used to diagnose glioma.

Accuracy is the most critical parameter in cancer diagnosis, which represents the ability to distinguish normal tissue from glioma tissue with different grades. To demonstrate the accuracy to distinguish between the normal tissue and different grades of glioma tissue via the Vis–NIR photodetectors, the machine learning method is adopted to explore the recognition accuracy under single-wavelength detection and multiwavelength detection. The support vector machine (SVM) was chosen because of its reliability and accuracy in small sample data set training.^{52,53} The data were collected by recording the photocurrents of the photodetectors under 5 V bias as typical wavelengths of light passing vertically through various regions of different tissue sections. Photocurrent data were further normalized by $I_{\text{effective}}/I_{\text{control}}$, where $I_{\text{effective}}$ is the photocurrent obtained by incident light passing through the tissue area and I_{control} is the photocurrent obtained by incident light passing through the blank area of the sections (Table S1). For single-model detection, four SVM models were trained using normalized photocurrent data at 450, 532, 650, and 980 nm as features, respectively. After shuffling the order of the data, 60% of the data was used for training, and the remaining 40% of the data was used to test the model accuracy (Figure 4h). This process was carried out 100 times in total. The results show that the accuracy of glioma tissue differentiation under a single wavelength is 98.7%, 77.1%, 84.5%, and 93.3%, respectively. After comprehensively using the data of the four typical wavelengths of light as features, the multimodal detection accuracy increases to 99.3% (Figure 4i). Sensitivity and specificity are another two important parameters for evaluating diagnostic performance. The diagnostic sensitivity under a single wavelength detection is 98.1%, 65.6%, 76.7%, and 90.0%, respectively (Table S2). The specificity of the Vis–NIR photodetectors under all four single-modal detections is 100%. The sensitivity and specificity under multimodal detection are 99.0% and 100%, respectively (Table S3). Besides accuracy, the multimodal detection effectively improves the sensitivity and specificity, as more features can be integrated and analyzed to enhance the distinction of different tissues. The high accuracy, sensitivity, and specificity demonstrate the potential of the side-wrapped lateral heterogeneous photodetectors with multimodal detection for rapid classification of glioma. The validation of the sensor and model was undertaken with a small number of clinical specimens. To realize the clinical glioma diagnosis, it is necessary to use a large number of double-blind specimens for clinical validation in future work.

CONCLUSION

In summary, we have fabricated side-wrapped lateral heterogeneous UCNP/ perovskite-based photodetectors through the sequential template-assisted printing strategy. The side-wrapped heterogeneous structure with UCNP exhibits excellent responsiveness to Vis–NIR light compared with the fully wrapped structure due to the sufficient photon absorption. Superior NIR and visible photodetection capabilities with R reaching 150 mA W⁻¹ at 980 nm and 1084 A W⁻¹ at 450 nm are demonstrated. The printed Vis–NIR

photodetectors are employed for glioma grade diagnosis by utilizing multimodal analysis for the absorbance of different grades of glioma across the Vis–NIR region. They provide a precise diagnosis with a detection accuracy of 99.3%. The printed biomedical photoelectric detection strategy can be further developed to assist clinicians in identifying the origin of tumors, which facilitates achieving surgical diagnosis and precise resection.

EXPERIMENTAL SECTION

Materials. Cesium iodide (CsI, >99.999% purity), lead(II) iodide (PbI₂, >99.999% purity), and lead(II) bromide (PbBr₂) were purchased from Xi'an Polymer Light Technology Corp. Dimethyl sulfoxide (DMSO) and 1,2-dichlorobenzene (o-DCB) were purchased from Sigma-Aldrich. All chemicals were used as purchased without further purification. The CsPbI_{2.2}Br_{0.8} precursor solution (5–80 mg mL⁻¹) was prepared by dissolving CsI, PbBr₂, and PbI₂ into a certain amount of DMSO in a molar ratio of 5:2:3 and stirring on a hot plate at 60 °C for 2 h. The up-conversion particle dispersion liquid (dispersed in toluene, 5 mg mL⁻¹) was purchased from Xi'an Ruixi Biological Technology Co., Ltd. and concentrated twice (dispersed in o-DCB, 10 mg mL⁻¹). The intraoperative frozen sections including normal tissue sections, grade II glioma tissue sections, and grade IV glioma tissue sections in this work were from the Chinese PLA General Hospital. There were five slices for each type. All experiments were performed in compliance with relevant Chinese and institutional laws and guidelines and were approved by the medical ethics committee of Chinese PLA General Hospital. Informed consent was obtained from all patients.

Fabrication. The 1D CsPbI_{2.2}Br_{0.8} arrays and 1D CsPbI_{2.2}Br_{0.8}/UCNPs arrays were prepared as follows. The line-shaped micropillar template (2 μm in width and 20 μm in separation) modified with 1H,1H,2H,2H-perfluorodecyltrimethoxysilane (80 °C, 2 h) was constructed to guide the assembly process. The Si/SiO₂ substrate covered by the as-prepared template was placed horizontally, and the pressure was applied to the printing system. A 5 μL CsPbI_{2.2}Br_{0.8} precursor solution was carefully injected into the sandwich structure formed by the substrate and template along the groove orientation. The sandwich system was kept in a vacuum oven heated at 110 °C for 2 h. The 1D CsPbI_{2.2}Br_{0.8} arrays were obtained on the substrate directly after detaching the template. For the generation of 1D CsPbI_{2.2}Br_{0.8}/UCNPs arrays, the up-conversion particle dispersion liquid was continuously injected along the groove orientation before the template was detached. The whole system was subsequently heated at 120 °C for 3 h and 150 °C for 3 h to ensure the total evaporation of the o-DCB solvent.

Characterization. The structures of 1D CsPbI_{2.2}Br_{0.8} arrays and 1D CsPbI_{2.2}Br_{0.8}/UCNPs arrays were characterized by SEM (S4800, Japan) at an accelerating voltage of 10.0 kV. The elemental analysis for the CsPbI_{2.2}Br_{0.8}/UCNPs 1D structure was carried out by EDS at an accelerating voltage of 15.0 kV. The UV–vis absorption spectrum was recorded on a UV–vis–NIR spectrophotometer (Shimadzu, UV-2600). The PL emission spectra were obtained by a fluorescence spectrometer (Edinburgh Instruments Ltd., FLS980) with an excitation wavelength of 980 nm. The optical images and fluorescence images were obtained by an optical microscope (Nikon, LV100ND) coupled to a charge-coupled device (CCD) camera. Confocal fluorescence images were obtained on a laser confocal microscope (NIS-Elements) by using excitation wavelengths of 488 and 561 nm. To distinguish the fluorescence of UCNP from perovskite arrays, sodium fluorescein (a green fluorescent dye) was added to the UCNP dispersion, while rhodamine B (a red fluorescent dye) was added to the perovskite precursor solution to enhance the fluorescence intensity. Contact angles were measured using a contact angle measurement device (OCA20, Germany) with DMSO on the SiO₂ surface. The height of 1D CsPbI_{2.2}Br_{0.8}/UCNPs arrays was tested using an optical profiler (ContourGT-K1).

Simulation. A pseudopotential two-phase lattice Boltzmann model combined with a nanoparticle transport model was applied

to simulate the evaporation and resultant secondary printing processes.^{47,48} To save computational resources, only one channel was modeled as a representation. The mechanism of multiple separated channels is the same. The bottom substrate and the solution are in light gray and blue, respectively. The first printed trapezoidal configuration is in yellow, while the template is in dark gray (with top). The evaporation occurring at the two open ends of the channel was induced by a pressure difference between the saturation vapor pressure at the liquid–gas interface and the open ends. The contact angle of the substrate and the first printed configuration was around 20°, while the rest is 80°. During the evaporation process, the liquid–gas interfaces receded at both ends. In the gap between the bottom substrate, the first printed configuration, and the template, the liquid film remained due to the capillary flow from the bulk. Meanwhile, the nanoparticles were transported to the capillary trailing and accumulated over there. The capillary trailing stayed until the complete evaporation of the bulk liquid. Afterward, the capillary trailing was gradually evaporated and the nanoparticles deposited upon the first printed configuration, forming the side-wrapped lateral heterogeneous structure.

Optoelectronic Performance Measurement. The photodetectors were fabricated by depositing a 100 nm Au layer on 1D CsPbI_{2.2}Br_{0.8}/UCNPs arrays through a mask.⁵⁰ The channel is 5 μm in length and 4 μm in width. The number of pixels of the photodetectors can reach 2 × 10⁴ pixels cm⁻². The optoelectronic performances of 1D CsPbI_{2.2}Br_{0.8}/UCNPs photodetector arrays at different wavelengths were recorded by a semiconductor system (Keithley 4200A-SCS) on a four-probe station (Ideaoptics Inc.). The power intensity of the incident laser was measured by an optical power meter (PM100D, Thorlabs).

Data Collection for Machine Learning. Typical wavelengths of laser lights (450, 532, 650, and 980 nm) were irradiated on the Vis–NIR photodetectors after transmitting through different regions of the three types of tissue sections. There were five slices for each type. The photocurrent data were collected under a 5 V bias. Data of 164 cases were collected from the effective area of the normal tissue section (64 cases with 450 nm, 36 cases with 532 nm, 36 cases with 650 nm, and 28 cases with 980 nm). Data of 186 cases were collected from the effective area of the tissue section of grade II gliomas (59 cases with 450 nm, 25 cases with 532 nm, 38 cases with 650 nm, and 64 cases with 980 nm). Data of 170 cases were collected from the effective area of the tissue section of grade IV gliomas (53 cases with 450 nm, 29 cases with 532 nm, 36 cases with 650 nm, and 52 cases with 980 nm). The photocurrent data were normalized by $I_{\text{effective}}/I_{\text{control}}$. The normalized photocurrent data were used as the data for training and testing.

Glioma Diagnosis by Machine Learning. Tissue recognition can be powered by various machine learning algorithms (Random Forest, Hidden Markov Models, Convolutional Neural Network, etc.). All can serve our purpose. Among them, SVM was chosen because of its reliability and accuracy in small sample data set training, which was a great fit for the demand. Features and information for training and classification were based on the different data of various wavelengths we collected. Under the single-model detection, four SVM models were trained using normalized photocurrent data at 450, 532, 650, and 980 nm as features, respectively. The multimodal detection model was trained by comprehensively using the data under four conditions of 450, 532, 650, and 980 nm as features. After shuffling the order of the data, 60% of the data was randomly selected for training and 40% for testing. This process was carried out 100 times in total. In this work, the accuracy rate, sensitivity, and specificity are defined as the ratio of the number of data judged to be correct to the total number of data collected from all tissues, the ratio of the data number correctly determined as glioma tissues (among the data collected from all glioma tissues) to the data number collected from all glioma tissues, and the ratio of the data number correctly determined as normal tissues (among the data collected from all normal tissues) to the data number collected from all normal tissues, respectively. The code for machine learning has been disclosed in [Code S1](#).

ASSOCIATED CONTENT

Supporting Information

The Supporting Information is available free of charge at <https://pubs.acs.org/doi/10.1021/acsnano.2c06004>.

Size distribution of UCNPs; absorption spectra; the radiative energy transfer; PL spectra; photoelectric performance comparison; contact angle of the printing system; fluid behavior simulation; *in situ* fluorescent microscopy images; optical and fluorescence microscope images; EDS analysis; assembly phase diagrams; width/height characterization; SEM images and *I*–*V* curves of the heterostructures with different wrapped widths; *I*–*V* curves and *I*–*t* response at various wavelengths, response time; detailed experimental data and results for glioma diagnosis (PDF)

Movie S1: Simulation of the flow behavior of UCNPs ink confined between the micropillar-structured template and the substrate (AVI)

Code S1: The code used for machine learning assisted analysis (PDF)

AUTHOR INFORMATION

Corresponding Authors

Qi Pan – Key Laboratory of Green Printing, CAS Research/Education Center for Excellence in Molecular Sciences, Institute of Chemistry, Chinese Academy of Sciences (ICCAS), Beijing Engineering Research Center of Nanomaterials for Green Printing Technology, Beijing National Laboratory for Molecular Sciences (BNLMS), Beijing 100190, China; Email: panqipanqi@iccas.ac.cn

Meng Su – Key Laboratory of Green Printing, CAS Research/Education Center for Excellence in Molecular Sciences, Institute of Chemistry, Chinese Academy of Sciences (ICCAS), Beijing Engineering Research Center of Nanomaterials for Green Printing Technology, Beijing National Laboratory for Molecular Sciences (BNLMS), Beijing 100190, China; University of Chinese Academy of Sciences, Beijing 100049, China; Email: sumeng1988@iccas.ac.cn

Yanlin Song – Key Laboratory of Green Printing, CAS Research/Education Center for Excellence in Molecular Sciences, Institute of Chemistry, Chinese Academy of Sciences (ICCAS), Beijing Engineering Research Center of Nanomaterials for Green Printing Technology, Beijing National Laboratory for Molecular Sciences (BNLMS), Beijing 100190, China; University of Chinese Academy of Sciences, Beijing 100049, China; orcid.org/0000-0002-0267-3917; Email: ylsong@iccas.ac.cn

Authors

Hongfei Xie – Key Laboratory of Green Printing, CAS Research/Education Center for Excellence in Molecular Sciences, Institute of Chemistry, Chinese Academy of Sciences (ICCAS), Beijing Engineering Research Center of Nanomaterials for Green Printing Technology, Beijing National Laboratory for Molecular Sciences (BNLMS), Beijing 100190, China; University of Chinese Academy of Sciences, Beijing 100049, China

Dongdong Wu – Department of Neurosurgery, The First Medical Centre, Chinese PLA General Hospital, Beijing 100853, China; Medical School of Chinese PLA Hospital, Beijing 100853, China

Feifei Qin – Department of Mechanical and Process Engineering, Swiss Federal Institute of Technology in Zürich (ETH Zürich), Zürich 8092, Switzerland; orcid.org/0000-0001-9121-4263

Shuoran Chen – Research Center for Green Printing Nanophotonic Materials, Suzhou University of Science and Technology, Suzhou 215009, China; orcid.org/0000-0002-5080-3640

Wei Sun – Institute of Software, Chinese Academy of Sciences, Beijing 100049, China

Xu Yang – Key Laboratory of Green Printing, CAS Research/Education Center for Excellence in Molecular Sciences, Institute of Chemistry, Chinese Academy of Sciences (ICCAS), Beijing Engineering Research Center of Nanomaterials for Green Printing Technology, Beijing National Laboratory for Molecular Sciences (BNLMS), Beijing 100190, China; University of Chinese Academy of Sciences, Beijing 100049, China

Sisi Chen – Key Laboratory of Green Printing, CAS Research/Education Center for Excellence in Molecular Sciences, Institute of Chemistry, Chinese Academy of Sciences (ICCAS), Beijing Engineering Research Center of Nanomaterials for Green Printing Technology, Beijing National Laboratory for Molecular Sciences (BNLMS), Beijing 100190, China; University of Chinese Academy of Sciences, Beijing 100049, China

Tingqing Wu – Key Laboratory of Green Printing, CAS Research/Education Center for Excellence in Molecular Sciences, Institute of Chemistry, Chinese Academy of Sciences (ICCAS), Beijing Engineering Research Center of Nanomaterials for Green Printing Technology, Beijing National Laboratory for Molecular Sciences (BNLMS), Beijing 100190, China; University of Chinese Academy of Sciences, Beijing 100049, China

Jimei Chi – Key Laboratory of Green Printing, CAS Research/Education Center for Excellence in Molecular Sciences, Institute of Chemistry, Chinese Academy of Sciences (ICCAS), Beijing Engineering Research Center of Nanomaterials for Green Printing Technology, Beijing National Laboratory for Molecular Sciences (BNLMS), Beijing 100190, China; University of Chinese Academy of Sciences, Beijing 100049, China

Zengqi Huang – Key Laboratory of Green Printing, CAS Research/Education Center for Excellence in Molecular Sciences, Institute of Chemistry, Chinese Academy of Sciences (ICCAS), Beijing Engineering Research Center of Nanomaterials for Green Printing Technology, Beijing National Laboratory for Molecular Sciences (BNLMS), Beijing 100190, China

Huadong Wang – Key Laboratory of Green Printing, CAS Research/Education Center for Excellence in Molecular Sciences, Institute of Chemistry, Chinese Academy of Sciences (ICCAS), Beijing Engineering Research Center of Nanomaterials for Green Printing Technology, Beijing National Laboratory for Molecular Sciences (BNLMS), Beijing 100190, China; University of Chinese Academy of Sciences, Beijing 100049, China

Zeyang Zhang – Key Laboratory of Green Printing, CAS Research/Education Center for Excellence in Molecular Sciences, Institute of Chemistry, Chinese Academy of Sciences (ICCAS), Beijing Engineering Research Center of Nanomaterials for Green Printing Technology, Beijing National Laboratory for Molecular Sciences (BNLMS),

Beijing 100190, China; University of Chinese Academy of Sciences, Beijing 100049, China

Bingda Chen – Key Laboratory of Green Printing, CAS Research/Education Center for Excellence in Molecular Sciences, Institute of Chemistry, Chinese Academy of Sciences (ICCAS), Beijing Engineering Research Center of Nanomaterials for Green Printing Technology, Beijing National Laboratory for Molecular Sciences (BNLMS), Beijing 100190, China; University of Chinese Academy of Sciences, Beijing 100049, China

Jan Carmeliet – Department of Mechanical and Process Engineering, Swiss Federal Institute of Technology in Zürich (ETH Zürich), Zürich 8092, Switzerland

Complete contact information is available at:
<https://pubs.acs.org/10.1021/acsnano.2c06004>

Author Contributions

Q.P., M.S., and Y.S. conceived and designed the experiments. H.X., D.W., S.C., X.Y., S.C., T.W., J.C., Z.H., H.W., Z.Z., and B.C. contributed to the experimental design and device fabrication. H.X. fabricated the devices and conducted the optoelectronic measurements. H.X. and Q.P. wrote the manuscript. M.S. and Y.S. modified it. F.Q., J.C., and W.S. contributed to the simulation and calculation sections. All authors reviewed the manuscript.

Funding

This work was supported by National Key R&D Program of China (Grant No. 2018YFA0208501), Beijing Nova Program from Beijing Municipal Science & Technology Commission (Grant Nos. Z201100006820037 and Z211100002121001), the National Natural Science Foundation of China (Grant Nos. 22075296, 52103310, 91963212, and 51961145102), the China Postdoctoral Science Foundation (Grant Nos. 2020TQ0325 and 2020M680679), and Beijing National Laboratory for Molecular Sciences (Grant No. BNLMS-CXXM-202005).

Notes

The authors declare no competing financial interest.

REFERENCES

- (1) Wang, S.; Zhang, L.; Zhao, J.; He, M.; Huang, Y.; Zhao, S. A Tumor Microenvironment-Induced Absorption Red-Shifted Polymer Nanoparticle for Simultaneously Activated Photoacoustic Imaging and Photothermal Therapy. *Sci. Adv.* **2021**, *7*, 3588.
- (2) Ji, C.; Zhao, M.; Wang, C.; Liu, R.; Zhu, S.; Dong, X.; Su, C.; Gu, Z. Biocompatible Tantalum Nanoparticles as Radiosensitizers for Enhancing Therapy Efficacy in Primary Tumor and Metastatic Sentinel Lymph Nodes. *ACS Nano* **2022**, *16*, 9428–9441.
- (3) Wang, H.; Chao, Y.; Zhao, H.; Zhou, X.; Zhang, F.; Zhang, Z.; Li, Z.; Pan, J.; Wang, J.; Chen, Q.; Liu, Z. Smart Nanomedicine to Enable Crossing Blood–Brain Barrier Delivery of Checkpoint Blockade Antibody for Immunotherapy of Glioma. *ACS Nano* **2022**, *16*, 664–674.
- (4) Zhang, J.; Chen, C.; Li, A.; Jing, W.; Sun, P.; Huang, X.; Liu, Y.; Zhang, S.; Du, W.; Zhang, R.; Liu, Y.; Gong, A.; Wu, J.; Jiang, X. Immunostimulant Hydrogel for the Inhibition of Malignant Glioma Relapse Post-Resection. *Nat. Nanotechnol.* **2021**, *16*, 538–548.
- (5) Li, W.; Ren, L.; Zheng, X.; Liu, J.; Wang, J.; Ji, T.; Du, G. 3-O-Acetyl-11-Keto-B-Boswellic Acid Ameliorated Aberrant Metabolic Landscape and Inhibited Autophagy in Glioblastoma. *Acta Pharm. Sin. B* **2020**, *10*, 301–312.
- (6) Jensen, S. A.; Day, E. S.; Ko, C. H.; Hurley, L. A.; Luciano, J. P.; Kouri, F. M.; Merkel, T. J.; Luthi, A. J.; Patel, P. C.; Cutler, J. I.; Daniel, W. L.; Scott, A. W.; Rotz, M. W.; Meade, T. J.; Giljohann, D.

- A.; Mirkin, C. A.; Stegh, A. H. Spherical Nucleic Acid Nanoparticle Conjugates as an Rnai-Based Therapy for Glioblastoma. *Sci. Transl. Med.* **2013**, *5*, 209ra152–209ra152.
- (7) Langen, K.-J.; Galdiks, N.; Hattingen, E.; Shah, N. J. Advances in Neuro-Oncology Imaging. *Nat. Rev. Neurol.* **2017**, *13*, 279–289.
- (8) Zhou, J.; Tryggestad, E.; Wen, Z.; Lal, B.; Zhou, T.; Grossman, R.; Wang, S.; Yan, K.; Fu, D.-X.; Ford, E.; Tyler, B.; Blakeley, J.; Lartera, J.; van Zijl, P. C. M. Differentiation between Glioma and Radiation Necrosis Using Molecular Magnetic Resonance Imaging of Endogenous Proteins and Peptides. *Nat. Med.* **2011**, *17*, 130–134.
- (9) Wiestler, B.; Kluge, A.; Lukas, M.; Gempt, J.; Ringel, F.; Schlegel, J.; Meyer, B.; Zimmer, C.; Förster, S.; Pyka, T.; Preibisch, C. Multiparametric Mri-Based Differentiation of Who Grade II/III Glioma and Who Grade IV Glioblastoma. *Sci. Rep.* **2016**, *6*, 35142.
- (10) Tosi, U.; Kommidi, H.; Adeuyan, O.; Guo, H.; Maachani, U. B.; Chen, N.; Su, T.; Zhang, G.; Pisapia, D. J.; Dahmane, N.; Ting, R.; Souweidane, M. M. Pet, Image-Guided Hdac Inhibition of Pediatric Diffuse Midline Glioma Improves Survival in Murine Models. *Sci. Adv.* **2020**, *6*, 4105.
- (11) Deuschl, C.; Kirchner, J.; Poepfel, T. D.; Schaarschmidt, B.; Kebir, S.; El Hindy, N.; Hense, J.; Quick, H. H.; Glas, M.; Herrmann, K.; Umütlu, L.; Moenninghoff, C.; Radbruch, A.; Forsting, M.; Schlamann, M. 11c–Met Pet/Mri for Detection of Recurrent Glioma. *Eur. J. Nucl. Med. Mol. Imaging* **2018**, *45*, 593–601.
- (12) Pauleit, D.; Floeth, F.; Hamacher, K.; Riemenschneider, M. J.; Reifenberger, G.; Müller, H.-W.; Zilles, K.; Coenen, H. H.; Langen, K.-J. O-(2-[18F]Fluoroethyl)-L-Tyrosine Pet Combined with Mri Improves the Diagnostic Assessment of Cerebral Gliomas. *Brain* **2005**, *128*, 678–687.
- (13) Shi, T.; Huang, C.; Li, Y.; Huang, F.; Yin, S. NIR-II Phototherapy Agents with Aggregation-Induced Emission Characteristics for Tumor Imaging and Therapy. *Biomaterials* **2022**, *285*, 121535.
- (14) Bergmann, F.; Foschum, F.; Marzel, L.; Kienle, A. Ex Vivo Determination of Broadband Absorption and Effective Scattering Coefficients of Porcine Tissue. *Photonics* **2021**, *8*, 365.
- (15) Wang, R.; Li, X.; Zhou, L.; Zhang, F. Epitaxial Seeded Growth of Rare-Earth Nanocrystals with Efficient 800 Nm near-Infrared to 1525 Nm Short-Wavelength Infrared Downconversion Photoluminescence for in vivo Bioimaging. *Angew. Chem., Int. Ed.* **2014**, *53*, 12086–12090.
- (16) Kong, J.; Zou, R.; Law, G.-L.; Wang, Y. Biomimetic Multifunctional Persistent Luminescence Nanoprobes for Long-Term near-Infrared Imaging and Therapy of Cerebral and Cerebellar Gliomas. *Sci. Adv.* **2022**, *8*, 7077.
- (17) Mehidine, H.; Chalumeau, A.; Poulon, F.; Jamme, F.; Varlet, P.; Devaux, B.; Refregiers, M.; Abi Haidar, D. Optical Signatures Derived from Deep UV to NIR Excitation Discriminates Healthy Samples from Low and High Grades Glioma. *Sci. Rep.* **2019**, *9*, 8786.
- (18) Shapey, J.; Xie, Y.; Nabavi, E.; Ebner, M.; Saeed, S. R.; Kitchen, N.; Dorward, N.; Grieve, J.; McEvoy, A. W.; Miserochi, A.; Grover, P.; Bradford, R.; Lim, Y.-M.; Ourselin, S.; Brandner, S.; Jaunmuktane, Z.; Vercauteren, T. Optical Properties of Human Brain and Tumour Tissue: An ex vivo Study Spanning the Visible Range to Beyond the Second near-Infrared Window. *J. Biophotonics* **2022**, *15*, 202100072.
- (19) Jacques, S. L. Optical Properties of Biological Tissues: A Review. *Phys. Med. Biol.* **2013**, *58*, 37.
- (20) Xiang, R.; Inoue, T.; Zheng, Y.; Kumamoto, A.; Qian, Y.; Sato, Y.; Liu, M.; Tang, D.; Gokhale, D.; Guo, J.; Hisama, K.; Yotsumoto, S.; Ogamoto, T.; Arai, H.; Kobayashi, Y.; Zhang, H.; Hou, B.; Anisimov, A.; Maruyama, M.; Miyata, Y.; Okada, S.; Chiashi, S.; Li, Y.; Kong, J.; Kauppinen, E. I.; Ikuhara, Y.; Suenaga, K.; Maruyama, S. One-Dimensional Van Der Waals Heterostructures. *Science* **2020**, *367*, 537–542.
- (21) Chen, S.; Teng, C.; Zhang, M.; Li, Y.; Xie, D.; Shi, G. A Flexible UV-Vis–NIR Photodetector Based on a Perovskite/Conjugated-Polymer Composite. *Adv. Mater.* **2016**, *28*, 5969–5974.
- (22) Zou, H.; Li, X.; Dai, G.; Peng, W.; Ding, Y.; Zhang, Y.; Wang, A. C.; Zhang, S. L.; Xu, C.; Zhang, S.-L. Dramatically Enhanced Broadband Photodetection by Dual Inversion Layers and Fowler–Nordheim Tunneling. *ACS Nano* **2019**, *13*, 2289–2297.
- (23) Zhou, Y.; Zhao, L.; Ni, Z.; Xu, S.; Zhao, J.; Xiao, X.; Huang, J. Heterojunction Structures for Reduced Noise in Large-Area and Sensitive Perovskite X-Ray Detectors. *Sci. Adv.* **2021**, *7*, 6716.
- (24) Zou, H.; Li, X.; Peng, W.; Wu, W.; Yu, R.; Wu, C.; Ding, W.; Hu, F.; Liu, R.; Zi, Y. Piezo-Phototronic Effect on Selective Electron or Hole Transport through Depletion Region of Vis–NIR Broadband Photodiode. *Adv. Mater.* **2017**, *29*, 1701412.
- (25) Lee, W. S.; Lee, S.-W.; Joh, H.; Seong, M.; Kim, H.; Kang, M. S.; Cho, K.-H.; Sung, Y.-M.; Oh, S. J. Designing Metallic and Insulating Nanocrystal Heterostructures to Fabricate Highly Sensitive and Solution Processed Strain Gauges for Wearable Sensors. *Small* **2017**, *13*, 1702534.
- (26) Kim, J.; Rhee, D.; Song, O.; Kim, M.; Kwon, Y. H.; Lim, D. U.; Kim, I. S.; Mazánek, V.; Valdman, L.; Sofer, Z.; Cho, J. H.; Kang, J. All-Solution-Processed Van Der Waals Heterostructures for Wafer-Scale Electronics. *Adv. Mater.* **2022**, *34*, 2106110.
- (27) Li, X.; Schaak, R. E. Size- and Interface-Modulated Metal–Insulator Transition in Solution-Synthesized Nanoscale Vo2-Tio2-Vo2 Heterostructures. *Angew. Chem., Int. Ed.* **2017**, *56*, 15550–15554.
- (28) Pan, S.; Zou, H.; Wang, A. C.; Wang, Z.; Yu, J.; Lan, C.; Liu, Q.; Wang, Z. L.; Lian, T.; Peng, J. Rapid Capillary-Assisted Solution Printing of Perovskite Nanowire Arrays Enables Scalable Production of Photodetectors. *Angew. Chem., Int. Ed.* **2020**, *59*, 14942–14949.
- (29) Wang, H.; Kim, D. H. Perovskite-Based Photodetectors: Materials and Devices. *Chem. Soc. Rev.* **2017**, *46*, 5204–5236.
- (30) Feng, J.; Gong, C.; Gao, H.; Wen, W.; Gong, Y.; Jiang, X.; Zhang, B.; Wu, Y.; Wu, Y.; Fu, H.; Jiang, L.; Zhang, X. Single-Crystalline Layered Metal-Halide Perovskite Nanowires for Ultra-sensitive Photodetectors. *Nat. Electron.* **2018**, *1*, 404–410.
- (31) Lan, C.; Zou, H.; Wang, L.; Zhang, M.; Pan, S.; Ma, Y.; Qiu, Y.; Wang, Z. L.; Lin, Z. Revealing Electrical-Poling-Induced Polarization Potential in Hybrid Perovskite Photodetectors. *Adv. Mater.* **2020**, *32*, 2005481.
- (32) Kim, H.-S.; Lee, C.-R.; Im, J.-H.; Lee, K.-B.; Moehl, T.; Marchioro, A.; Moon, S.-J.; Humphry-Baker, R.; Yum, J.-H.; Moser, J. E.; Grätzel, M.; Park, N.-G. Lead Iodide Perovskite Sensitized All-Solid-State Submicron Thin Film Mesoscopic Solar Cell with Efficiency Exceeding 9%. *Sci. Rep.* **2012**, *2*, 591.
- (33) Jeon, N. J.; Noh, J. H.; Yang, W. S.; Kim, Y. C.; Ryu, S.; Seo, J.; Seok, S. I. Compositional Engineering of Perovskite Materials for High-Performance Solar Cells. *Nature* **2015**, *517*, 476–480.
- (34) Park, Y. I.; Lee, K. T.; Suh, Y. D.; Hyeon, T. Upconverting Nanoparticles: A Versatile Platform for Wide-Field Two-Photon Microscopy and Multi-Modal in vivo Imaging. *Chem. Soc. Rev.* **2015**, *44*, 1302–1317.
- (35) Porter, J. F. Fluorescence Excitation by the Absorption of Two Consecutive Photons. *Phys. Rev. Lett.* **1961**, *7*, 414–415.
- (36) Xomalis, A.; Zheng, X.; Chikkaraddy, R.; Koczor-Benda, Z.; Miele, E.; Rosta, E.; Vandenbosch, G. A. E.; Martínez, A.; Baumberg, J. J. Detecting Mid-Infrared Light by Molecular Frequency Upconversion in Dual-Wavelength Nanoantennas. *Science* **2021**, *374*, 1268–1271.
- (37) Martini, L.; Chen, Z.; Mishra, N.; Barin, G. B.; Fantuzzi, P.; Ruffieux, P.; Fasel, R.; Feng, X.; Narita, A.; Coletti, C.; Müllen, K.; Candini, A. Structure-Dependent Electrical Properties of Graphene Nanoribbon Devices with Graphene Electrodes. *Carbon* **2019**, *146*, 36–43.
- (38) Zhou, Z.; Zhao, J.; Du, Y.; Wang, K.; Liang, J.; Yan, Y.; Zhao, Y. S. Organic Printed Core–Shell Heterostructure Arrays: A Universal Approach to All-Color Laser Display Panels. *Angew. Chem., Int. Ed.* **2020**, *59*, 11814–11818.
- (39) Xue, J.; Gu, Y.; Shan, Q.; Zou, Y.; Song, J.; Xu, L.; Dong, Y.; Li, J.; Zeng, H. Constructing Mie-Scattering Porous Interface-Fused Perovskite Films to Synergistically Boost Light Harvesting and Carrier Transport. *Angew. Chem., Int. Ed.* **2017**, *56*, 5232–5236.
- (40) Li, J.; Shen, Y.; Liu, Y.; Shi, F.; Ren, X.; Niu, T.; Zhao, K.; Liu, S. F. Stable High-Performance Flexible Photodetector Based on

Upconversion Nanoparticles/Perovskite Microarrays Composite. *ACS Appl. Mater. Interfaces* **2017**, *9*, 19176–19183.

(41) Zhang, X.; Yang, S.; Zhou, H.; Liang, J.; Liu, H.; Xia, H.; Zhu, X.; Jiang, Y.; Zhang, Q.; Hu, W.; Zhuang, X.; Liu, H.; Hu, W.; Wang, X.; Pan, A. Perovskite-Erbium Silicate Nanosheet Hybrid Waveguide Photodetectors at the near-Infrared Telecommunication Band. *Adv. Mater.* **2017**, *29*, 1604431.

(42) Su, M.; Song, Y. Printable Smart Materials and Devices: Strategies and Applications. *Chem. Rev.* **2022**, *122*, 5144–5164.

(43) Feng, J.; Song, Q.; Zhang, B.; Wu, Y.; Wang, T.; Jiang, L. Large-Scale, Long-Range-Ordered Patterning of Nanocrystals via Capillary-Bridge Manipulation. *Adv. Mater.* **2017**, *29*, 1703143.

(44) Sutton, R. J.; Eperon, G. E.; Miranda, L.; Parrott, E. S.; Kamino, B. A.; Patel, J. B.; Hörantner, M. T.; Johnston, M. B.; Haghighirad, A. A.; Moore, D. T.; Snaith, H. J. Bandgap-Tunable Cesium Lead Halide Perovskites with High Thermal Stability for Efficient Solar Cells. *Adv. Energy Mater.* **2016**, *6*, 1502458.

(45) Lin, Q.; Armin, A.; Burn, P. L.; Meredith, P. Filterless Narrowband Visible Photodetectors. *Nat. Photonics* **2015**, *9*, 687–694.

(46) Wang, Q.; Smith, J. A.; Skroblin, D.; Steele, J. A.; Wolff, C. M.; Caprioglio, P.; Stolterfoht, M.; Köbler, H.; Li, M.; Turren-Cruz, S.-H.; Gollwitzer, C.; Neher, D.; Abate, A. Managing Phase Purities and Crystal Orientation for High-Performance and Photostable Cesium Lead Halide Perovskite Solar Cells. *Solar RRL* **2020**, *4*, 2000213.

(47) Qin, F.; Del Carro, L.; Moqaddam, A. M.; Kang, Q.; Brunschweiler, T.; Derome, D.; Carmeliet, J. Study of Non-Isothermal Liquid Evaporation in Synthetic Micro-Pore Structures with Hybrid Lattice Boltzmann Model. *J. Fluid Mech.* **2019**, *866*, 33–60.

(48) Qin, F.; Su, M.; Zhao, J.; Moqaddam, A. M.; Del Carro, L.; Brunschweiler, T.; Kang, Q.; Song, Y.; Derome, D.; Carmeliet, J. Controlled 3d Nanoparticle Deposition by Drying of Colloidal Suspension in Designed Thin Micro-Porous Architectures. *Int. J. Heat Mass Transfer* **2020**, *158*, 120000.

(49) Feng, J.; Yan, X.; Liu, Y.; Gao, H.; Wu, Y.; Su, B.; Jiang, L. Crystallographically Aligned Perovskite Structures for High-Performance Polarization-Sensitive Photodetectors. *Adv. Mater.* **2017**, *29*, 1605993.

(50) Li, S.-X.; Xu, Y.-S.; Li, C.-L.; Guo, Q.; Wang, G.; Xia, H.; Fang, H.-H.; Shen, L.; Sun, H.-B. Perovskite Single-Crystal Microwire-Array Photodetectors with Performance Stability Beyond 1 Year. *Adv. Mater.* **2020**, *32*, 2001998.

(51) Wang, H.-P.; Li, S.; Liu, X.; Shi, Z.; Fang, X.; He, J.-H. Low-Dimensional Metal Halide Perovskite Photodetectors. *Adv. Mater.* **2021**, *33*, 2003309.

(52) Kim, M.; Chen, C.; Wang, P.; Mulvey, J. J.; Yang, Y.; Wun, C.; Antman-Passig, M.; Luo, H.-B.; Cho, S.; Long-Roche, K.; Ramanathan, L. V.; Jagota, A.; Zheng, M.; Wang, Y.; Heller, D. A. Detection of Ovarian Cancer via the Spectral Fingerprinting of Quantum-Defect-Modified Carbon Nanotubes in Serum by Machine Learning. *Nat. Biomed. Eng.* **2022**, *6*, 267–275.

(53) Zhou, K.; Liu, Y. Early-Stage Gas Identification Using Convolutional Long Short-Term Neural Network with Sensor Array Time Series Data. *Sensors* **2021**, *21*, 4826.

Recommended by ACS

Intelligent Nanotransducer for Deep-Tumor Hypoxia Modulation and Enhanced Dual-Photosensitizer Photodynamic Therapy

Youbin Li, Songjun Zeng, *et al.*

MARCH 22, 2022
ACS APPLIED MATERIALS & INTERFACES

[READ](#)

Low Toxicity, High Resolution, and Red Tissue Imaging in the Vivo of Yb/Tm/GZO@SiO₂ Core-Shell Upconversion Nanoparticles

Yandong Bai, Yongmei Li, *et al.*

MARCH 02, 2020
ACS OMEGA

[READ](#)

Sub-20 nm LiErF₄-Based Upconversion Nanophosphors for Simultaneous Imaging and Photothermal Therapeutics

A-Ra Hong, Ho Seong Jang, *et al.*

JULY 14, 2020
ACS APPLIED NANO MATERIALS

[READ](#)

Enhanced Upconversion Luminescence-Guided Synergistic Antitumor Therapy Based on Photodynamic Therapy and Immune Checkpoint Blockade

Bi Lin, Ruichan Lv, *et al.*

APRIL 22, 2020
CHEMISTRY OF MATERIALS

[READ](#)

[Get More Suggestions >](#)